Journal of Materials Chemistry C

ROYAL SOCIETY OF CHEMISTRY

PAPER

View Article Online
View Journal | View Issue

Cite this: J. Mater. Chem. C, 2021, 9, 14351

Ferroelectric perovskite-enhanced photoelectrochemical immunoassay with the photoexcited charge-transfer of a built-in electric field†

Zhichao Yu,[a] Jianhui Xu,[a] Yuxuan Li,[a] Hexiang Gong,[a] Qiaohua Wei *[a] and Dianping Tang *[ab]

Received 3rd July 2021,
Accepted 19th September 2021

DOI: 10.1039/d1tc03097c

rsc.li/materials-c

Efficient separation of photo-induced electrons and holes in the photoelectrochemical (PEC) sensors plays an important role in improving detection sensitivity. Based on this point, we report a simple and sensitive photoelectrochemical bioassay for prostate-specific antigen (PSA) detection using lanthanide-doped bismuth ferrite/reduced graphene oxide/tungsten oxide nanohybrids (BLFO/rGO/WO_3) as the photo-sensing material. Initially, WO_3 was excited under the continuous illumination to generate photo-induced electron–hole pairs. Then, rGO (as a suitable charge transfer medium) could effectively build a bridge between WO_3 and BLFO. With the mediation of the built-in electric field in BLFO, the transferred charges were allowed for directional migration in the circuit, thus achieving an effective separation of the photogenerated electron–hole pairs. Coupling with the amplification of enzymatic production (H_2O_2) and specific recognition of antigen–antibody immunoreaction, target concentration was relative to the corresponding photocurrent, thereby realizing the PSA sensitive detection. Under optimal conditions, the PEC immunoassay exhibited a good linear relationship within a dynamic working range from 0.1 ng mL^{-1} to 200 ng mL^{-1} with a detection limit of 49.4 pg mL^{-1}. In addition, this study afforded satisfying specificity, reproducibility, and long-term storage, which also matched well with the commercial PSA ELISA kit.

Introduction

Driven by the growing emphasis on health management and disease diagnosis, the sensitive and accurate detection of biomarkers has been deployed in numerous sensing strategies that are expected to reduce the reliance on expensive equipment and complicated operations.[1–4] Photoelectrochemical (PEC) biosensors have attracted increasing attention in recent years because of their high sensitivity, simple structure and operation, and wide response range.[5–12] In general, PEC biosensors need appropriate photoelectric electrodes as the sensing platforms to adapt to the specific probes and recognition events. Due to the low photon utilization efficiency and rapid complexation of photo-generated electron–hole pairs at single photoactive substances, some strategies are generally applied to improve the performance of photoelectronic materials, such as constituting homogeneous junctions[13] and heterogeneous junctions,[14] doping with noble metals,[15] dye sensitization[16] and shape engineering.[17,18] Although it has been shown that two-dimensional (2D) van der Waals heterojunctions and higher order 2D superlattices can availably break through the material range boundaries, they are approaching a bottleneck due to the intractability of most materials.[19] Therefore, it is necessary and tricky to develop new strategies to improve the photon utilization and electron–hole pairs mobility of photoelectronic semiconductors.

In terms of charge separation, ferroelectric materials are expected to be new players for building photoelectric electrodes due to their special built-in electric fields. To date, ferroelectric materials such as $[KNbO_3]_{1-x}[BaNi_{1/2}Nb_{1/2}O_{3-\delta}]_x$,[20] the classical perovskite $BaTiO_3$[21] and the organic ferroelectric perovskite $CH_3NH_3PbI_3$[22,23] have been successfully applied to PEC bioanalysis due to their excellent photoelectric conversion properties. However, the traditional heterojunctions of ferroelectric materials always suffer from the problem that the high concentration of free charges in the charge collector inevitably

[a] Key Laboratory for Analytical Science of Food Safety and Biology (MOE & Fujian Province), Fujian Provincial Key Laboratory of Electrochemical Energy Storage Materials, State Key Laboratory of Photocatalysis on Energy and Environment, Department of Chemistry, Fuzhou University, Fuzhou 350108, China. E-mail: qhw76@fzu.edu.cn, Dianping.tang@fzu.edu.cn
[b] Chongqing Vocational Institute of Engineering, Chongqing 402260, China

† Electronic supplementary information (ESI) available: Experimental section and optimization of experimental conditions. See DOI: 10.1039/d1tc03097c

shields the built-in electric field, jeopardizing the performances of the PEC sensors.[24–26] A direct way to solve this issue is to avoid excess electrons in ferroelectric materials by inserting electron collectors with the moderate free electron concentration between ferroelectric materials and photoelectric semiconductors. Importantly, Chen *et al.* reported a method for tuning the interfacial electron energy level by ferroelectric polarization to obtain a remarkable performance gain.[27] The use of graphene as an intermediate sandwich layer helps to balance carrier collection and charge screening in the piezoelectric and ferroelectric devices. Inspired by this study, there is no doubt that the new electrode structure, ferroelectric thin film-graphene-photosensitive semiconductor, can serve the construction of PEC sensors. In addition, lanthanum-doped bismuth ferrate (BLFO) is used for the demonstration due to its excellent ferroelectric stability and large remnant polarization.[28,29]

On the other hand, the selection of the photoelectric semiconductor is also an essential part for the construction of the photoactive electrode. Tungsten trioxide (WO_3), an n-type semiconductor (~2.6 eV), has drawn attention as a semiconductor, owing to its good photocorrosion inhibition and excellent electron transport properties.[30–32] However, the pristine state of WO_3 has relatively low photoelectric activity due to its high electron–hole pair complexation and low photon absorbance. The construction of heterojunctions is a dominant method to solve these defects, which is the most commonly used modification method. In a previous study, we synthesized WO_3–Au–CdS nanocomposites as the photosensitive material, and designed a solid metal-mediated *Z*-Scheme photoelectrochemical immunoassay for prostate-specific antigen (PSA), where the special heterojunction structure effectively enhanced the photocurrent.[3] To the best of our knowledge, there is no report focusing on electron collectors through tuning the electric field of ferroelectric materials to enhance the PEC bioanalytical platform for photosensitive substances.

In this study, we report the proof-of-concept of facile strategy for enhancing PEC biosensors that depends on an unique electrode structure. Different from the traditional photoelectrochemical biosensors, BLFO and WO_3 are immobilized on the electrode by layer-by-layer coating, and rGO was introduced as the intermediate interlayer to rapidly separate the electrons and holes generated by WO_3. In addition, a classical sandwich-type immunoassay model is designed in the detection strategy, as shown in Scheme 1. Initially, detachable polystyrene highly conjugated microplates coated with the anti-PSA monoclonal antibody (mAb_1) are used as the sites for immunoreaction. Sandwich immune complexes are then formed between target PSA and glucose oxidase-labeled anti-PSA polyclonal antibody (pAb_2). The enzymatic product hydrogen peroxide is obtained upon the addition of glucose, which is transferred to the photodetection cell as the light sacrificial agent. This classical enzyme-linked immunoreaction can significantly increase the photocurrent, so that the hydrogen peroxide concentration is proportional to the PSA concentration, enabling the sensitive detection of PSA. The introduction of BLFO is expected to improve

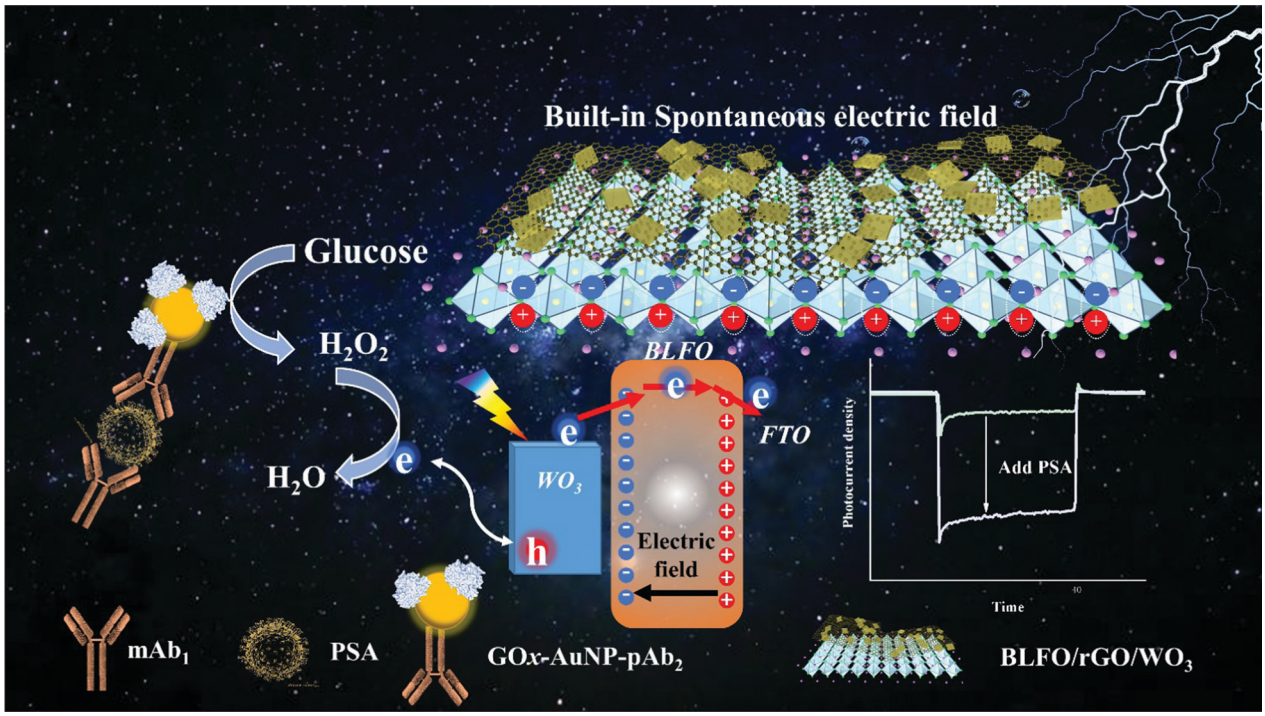

Scheme 1 Schematic illustration of the ferroelectric perovskite-enhanced photoelectrochemical immunoassay with photoexcited charge-transfer of built-in electric field for the monitoring of prostate-specific antigen (PSA) (BLFO: lanthanum-doped bismuth ferrate; rGO: reduced graphene oxide; WO_3: Tungsten trioxide; mAb_1: monoclonal anti-PSA capture antibody; pAb_2: polyclonal anti-PSA detection antibody; AuNP: Au nanoparticle; GOx: glucose oxidase).

PEC immunoassay sensitivity and versatility, contributing to the application of ferroelectric materials in PEC biosensing.

Experimental section

Synthesis of the ferroelectric perovskite BLFO film

BLFO film was prepared on a FTO substrate *via* a one-step liquid-phase synthesis and annealing treatment. Initially, 1.3606 g of bismuth nitride [$Bi(NO_3)_3{\cdot}5H_2O$], 1.2120 g of iron nitrate [$Fe(NO_3)_3{\cdot}9H_2O$], and 0.1948 g of lanthanum nitrate [$La(NO_3)_3{\cdot}6H_2O$] were dissolved in 4.0 mL of 2-methoxyethanol. A slight excess of bismuth nitrate was used to compensate for the loss of Bi during the annealing process. Then, 2.0 mL of acetic acid and 3.0 mL of acetic anhydride were added to the solution as a dehydrating agent, stirring at a medium speed throughout the process. Finally, 0.1 mL of ethanolamine was added and the volume was adjusted to 10 mL using 2-methoxyethanol. The precursor solution was stirred vigorously for 12 h. The obtained BLFO precursor solution was spin-coated onto the FTO electrode. The obtained sample was transferred to a muffle furnace for pyrolysis at 350 °C for 5 min, and then the temperature was raised to 600 °C for annealing for 20 min to obtain a uniform brownish yellow thin film of BLFO on the FTO electrode surface.

Synthesis of GO and rGO

The synthesis of GO was carried out according to the Hummers' method with slight modification.[7] The operation was briefly described as follows: 0.5 g of graphite powder and 1.0 g of sodium nitrate were added to 30 mL of concentrated sulfuric acid and stirred in the ice-water bath for 15 min. Subsequently, 3.0 g of potassium permanganate was added and stirred in the ice-water bath for 60 min. The above solution was transferred to a 35 °C water bath and stirred for 30 min, followed by the addition of 40 mL of ultrapure water and stirring for 30 min. 30% H_2O_2 was slowly added to the above the solution until the colour of the liquid changed to yellow. Finally, the suspension was centrifuged several times and washed with ultrapure water to neutral, and dried under vacuum at 60 °C.

The rGO dispersion solution was prepared by the thermal reduction method. The as-synthesized GO (8.0 mg mL^{-1}) was first dispersed by ultrasonication for 30 min. The dispersed graphene solution was transferred to an autoclave and kept in an oven at 200 °C for 16 h. After that, the autoclave was removed and the solution was cooled quickly to prevent overreaction. The obtained rGO was subjected to sonication before further processing.

Synthesis of WO_3 nanoplates

The synthesis of WO_3 nanoplates was achieved by a facile one-pot hydrothermal method. Initially, 3.0 g of sodium tungstate dihydrate was dissolved in 30 mL of ultrapure water and then transferred to a 120 mL autoclave with a Teflon liner. 15 mL of 35% hydrochloric acid was added to the solution at room temperature under vigorous stirring. After that, the autoclave was transferred to an oven for heat treatment at 180 °C for 8 h. After natural cooling, the solution was centrifuged and washed several times with ethanol and deionized water until it was nearly neutral. Lastly, the product was dried in a vacuum oven at 70 °C and collected for storage.

Preparations of the BLFO/rGO/WO_3 composite photoelectrode

The fabrication of the photoelectrode was mainly achieved by the drop coating technique. The obtained rGO and WO_3 nanoplates were diluted and sonicated to facilitate drop coating and to obtain refined photoelectrode. The obtained BLFO precursor solution was spin-coated onto the FTO electrode (2000 rpm, 30 s). The obtained sample was transferred to a muffle furnace for pyrolysis at 350 °C for 5 min, and then the temperature was raised to 600 °C for annealing for 20 min to obtain a uniform brownish yellow thin film of BLFO on the FTO electrode surface. 100 μL of the as-synthesized rGO precursor solution was fixed to 5 mL, and sonicated vigorously for 20 min. 40 μL of the diluted rGO solution was drop-coated onto the FTO/BLFO electrode and dried in a vacuum drying oven at 60 °C. Similarly, 0.0250 g of the as-synthesized WO_3 nanoplates was dissolved in 1.0 mL of ultrapure water and sonicated. 10 μL of the as-prepared WO_3 solution was coated dropwise on the FTO/BLFO/rGO electrode and dried in an oven to obtain the photoelectric working electrode.

Photoelectrochemical measurement

The photoelectric response of the PEC sensor was measured in a three-electrode system using a CHI 430A electrochemical workstation (Chenhua, Shanghai, China). The as-prepared electrode, Pt wire, and Ag/AgCl electrode were used as the working electrode, counter electrode, and reference electrode, respectively. Photocurrents were measured under the irradiation of a Xenon lamp (500 W). Different concentrations of PSA were configured prior to the analysis, and then PEC measurements were performed on the assembled electrodes at room temperature. The method of constructing antigen–antibody immune sandwich complexes and condition optimization experiments are shown in the ESI.†

Results and discussion

Structural and compositional characterization

In this study, the successful preparations of ferroelectric thin films and photosensitive materials were essential for the construction of the PEC platform. Therefore, the synthesis of BLFO thin films with excellent ferroelectric properties, fully exfoliated rGO, and WO_3 nanoplates were the focuses of this study. Scanning electron microscopy (SEM) was used in this study to obtain the microstructures of the as-synthesized materials and characterize the structure of the constructed electrodes. Fig. 1A schematically illustrates the three-dimensional structure of the as-fabricated FTO/BLFO/rGO/WO_3 electrode device. As shown in Fig. 1B, the BLFO film grown on the FTO electrode showed a neat arrangement, and

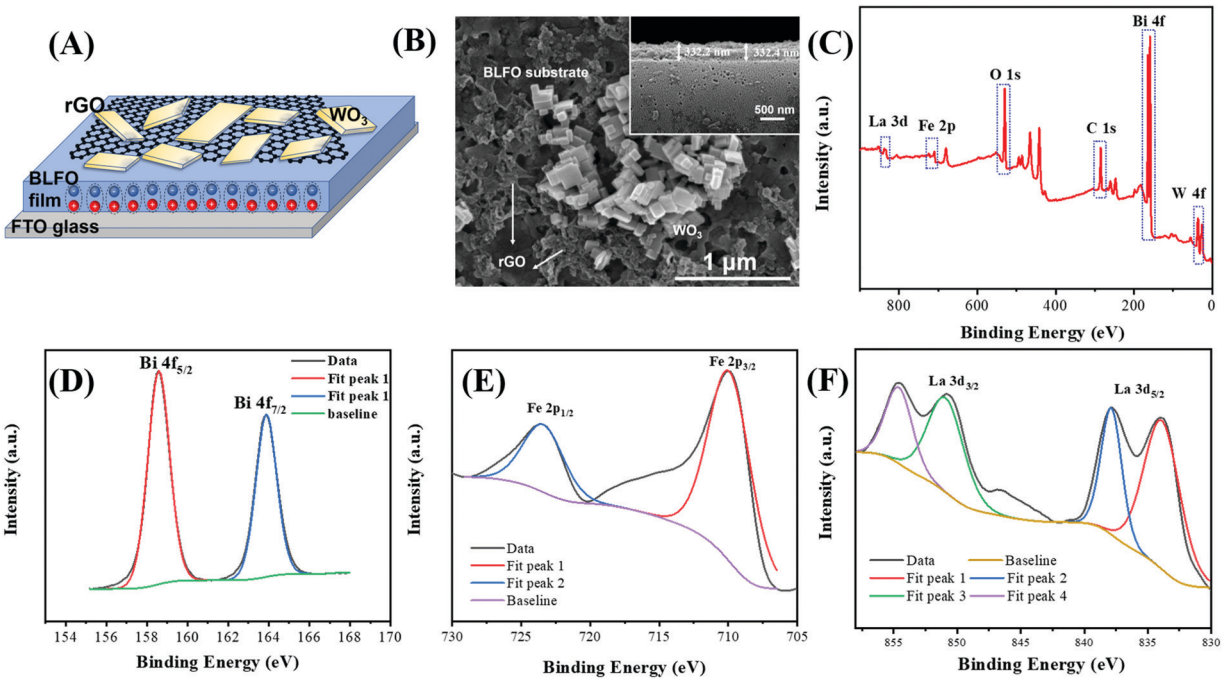

Fig. 1 (A) Schematic diagram of BLFO/rGO/WO_3 structure; (B) SEM image of BLFO/rGO/WO_3 surfaces (inset: cross-sectional SEM image of BLFO); (C) XPS patterns of composite electrodes; and (D–F) high-resolution XPS spectra of (D) Bi 4f, (E) Fe 2p and (F) La 3d.

the rGO attached to the BLFO surface showed a curved edge with a thickness of about 20 nm, which was the typical morphological feature of rGO.[33,34] The appearance of holes in the BLFO film might have originated from the overflow of organic compounds during the annealing process, which was normal in the synthesis of BLFO.[29] As shown in the cross-sectional SEM image (Fig. 1B, inset), the thickness of the ferroelectric film spin-coated on the FTO electrode was 332 nm. Moreover, we also characterized the morphology of the as-synthesized WO_3 and rGO *via* transmission electron microscopy (TEM). As shown in Fig. S1 (ESI†), the rGO was the monolayer, and the morphology of WO_3 showed a regular nanoplate structure.

In addition, the elemental analysis of films was carried out *via* X-ray photoelectron spectroscopy (XPS; Thermo Scientific K-Alpha). Fig. 1C shows the peaks of La, Fe, O, Bi, and W, which indicated the presence of these elements in the as-prepared products. As depicted in Fig. S2 (ESI†), the binding energy for W $4f_{5/2}$ and W $4f_{7/2}$ was at 37.5 and 35.3 eV, respectively, which concurred well to the previous results.[35] Fig. 1D–F show the binding energies of Bi 4f and Fe 2p peaks. They were concentrated at 164.9 (Bi $4f_{5/2}$), 158.5 eV (Bi $4f_{7/2}$), 723.2 eV (Fe $2p_{1/2}$), and 709.9 eV (Fe $2p_{3/2}$), respectively, which were characteristic values for Bi and Fe species in the perovskite.[36] It could be seen in Fig. 1F that the peaks with the binding energies of 833.9 and 850.9 eV, which belonged to La $3d_{5/2}$ and La $3d_{3/2}$, respectively. The energy difference between the La $3d_{3/2}$ and La $3d_{5/2}$ states was about 18 eV, which was similar to the energy difference of La doped in $BiFeO_3$.[37] In addition, we could clearly observe the appearance of a unique satellite peak associated with La $3d_{5/2}$ at the higher binding energy at 837.9 eV and another one associated with La $3d_{3/2}$ at 854.6 eV. The above-obtained results indicated that the expected photoelectrode was successfully constructed.

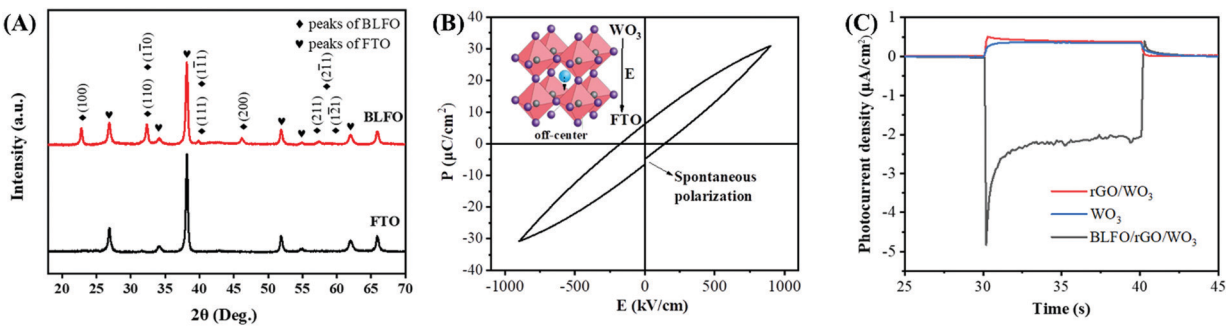

Fig. 2 (A) XRD patterns of FTO substrate and BLFO ferroelectric film; (B) ferroelectric hysteresis loop of the BLFO film (inset: the spontaneous polarization direction of the ferroelectric film); and (C) photocurrent responses of rGO/WO_3, WO_3, and BLFO/rGO/WO_3.

Characterization of ferroelectric properties

To understand the ferroelectric behavior of the as-synthesized BLFO films and their role in PEC, X-ray diffraction (XRD) and ferroelectric analysis were performed. Fig. 2A presents the XRD pattern of the BLFO film. The regular and shape of the diffraction peaks indicated that the film was well formed. In addition, no secondary phase spurious peaks appeared in the detection range of the diffractometer, which indicated that the BLFO film was successfully synthesized *via* the liquid-phase synthesis and spin-coating thermal annealing. We also observed the merging of the (110)/(1$\bar{1}$0) peaks, which indicated the distortion of the original perovskite structure. This phenomenon mainly was attributed to the distortion of the structure caused by the doping of La into the position of Bi, and it was worth noting that this distortion was beneficial to improve the ferroelectric properties.[29] To further demonstrate that the as-synthesized material is ferroelectric, we performed electrical hysteresis loop measurements on the BLFO films with the measured frequency of 10 kHz. We focused on the point in the figure, where the curve intersects the *Y*-axis, and it is clear from the Fig. 2B that when the electric field was 0, the curve data started at about -10 μC cm^{-2} in the negative direction with the *Y*-axis. Although the shape of the hysteresis line was not saturated, which was related to the polarization conditions, it was a direct evidence that the material was ferroelectric without polarization at room temperature.[29,38]

The separation of photogenerated electrons and holes and the corresponding enhancement of photocurrent could also be used to describe the ferroelectric behaviour of the film. As shown in Fig. 2C, the WO_3 nanosheets and rGO/WO_3 nanosheets showed weak photocurrent responses of 369.7 nA cm^{-2} and 432.0 nA cm^{-2}, respectively, while BLFO/rGO/WO_3 showed significantly enhanced photocurrent. Importantly, the photocurrent of WO_3 was converted from anodic to cathodic photocurrent after the introduction of BLFO, which possibly was due to the opposite direction of the self-polarizing electric field of BLFO and electron movement. This was consistent with the results of the electric hysteresis lines. The above-mentioned results showed that the as-synthesized BLFO has the property of spontaneous polarization and the ferroelectric field could effectively improve the charge separation of the photoelectrode.

Analytical performance of the PEC immunosensing platform

To explore the performance of the as-prepared photoelectrode for the detection of target PSA, a photoelectrochemical biosensor was constructed. The photocurrent was observed continuously in a detection cell containing 0.1 M Na_2SO_4 in the presence or absence of 2.0 ng mL^{-1} PSA. The results are depicted in Fig. 3A. The ferroelectric material-modified electrode had a larger photocurrent change than the electrode with only a single photoelectric semiconductor WO_3, which indicated that the ferroelectric field-mediated photoelectric electrode had a better charge separation efficiency. More profoundly, the ferroelectric material coupled with rGO could cause a huge rearrangement of the free carriers in the WO_3 layer, resulting in a larger width of the depletion region and several-fold increase in photocurrent.[27] In addition, photoactive semiconductor materials were excited to

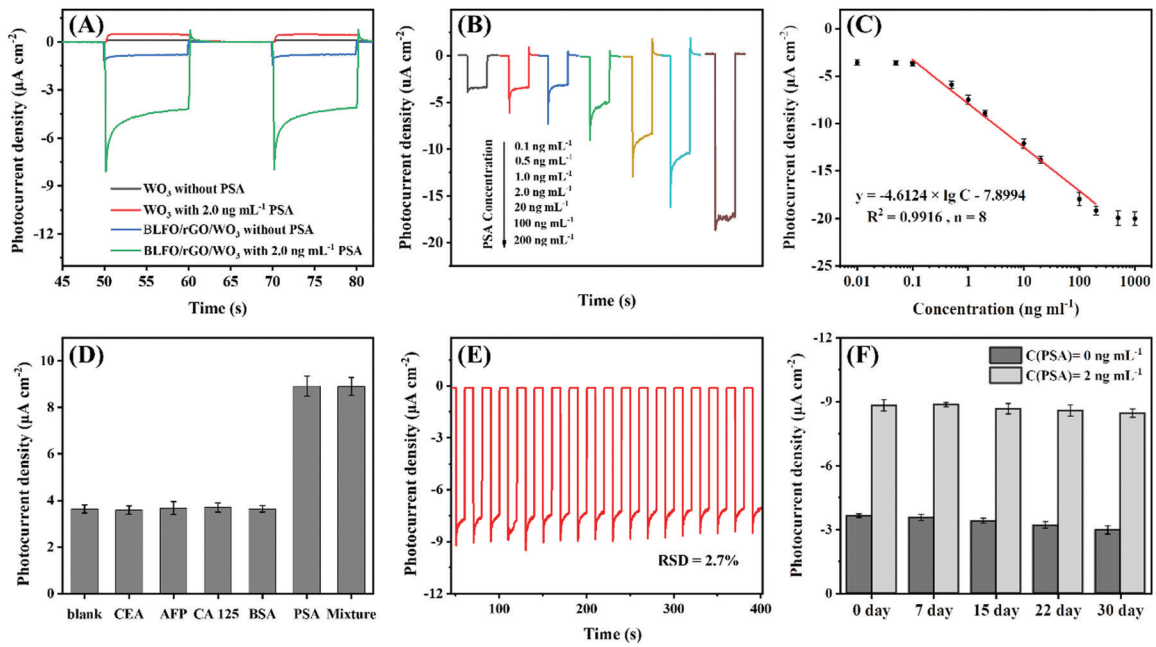

Fig. 3 (A) Photocurrents of WO_3 and composite BLFO/rGO/WO_3 in the absence and presence of target PSA (2.0 ng mL^{-1}); (B) photocurrents of the PEC immunosensing system based on BLFO/rGO/WO_3 for different-concentration PSA standards; (C) the corresponding calibration curve; (D) the specificity of the immunosensing system against PSA, CEA, AFP, CA-125, and BSA (the concentration of interfering substances was 50 ng mL^{-1}, and the concentration of PSA was 2.0 ng mL^{-1}); (E) the stability of the PEC immunosensing system; (F) photocurrents in the presence of target PSA (2.0 ng mL^{-1}) and absence of target PSA for 0–30 days.

Table 1 Comparison of different detection schemes for PSA detection (dynamic range: ng mL^{-1}; LOD: pg mL^{-1})

Detection method	Dynamic range	LOD	Ref.
Electrochemical aptasensor	0.01–500	1.24	40
Fluorescence sensor	0.1–10	10	41
Capacitance sensor	0.1–50	57	42
Impedimetric immunosensor	0.001–10	0.48	31
Acoustic resonator sensor	1–10	340	43
Surface–enhanced Raman spectroscopy	0.1–20	100	44
PEC immunoassay	0.001–8	0.52	45
PEC immunoassay	0.05–40	16.3	46
PEC immunoassay	0.1–200	49.4	This work

generate electrons and holes, which moved directionally towards the surface of the electrode to output an electrical signal under the modulation of the ferroelectric electric field. The spike-shaped photocurrent was mainly due to the compounding of electrons and holes in the bulk phase. In general, the dissolved oxygen or other active substances in the water might change the size and shape of the photocurrent.[39] On the other hand, the influx of carriers for a long time might have changed the spontaneously polarized ferroelectric domains arranged in a single direction in the BLFO, thus weakening the ferroelectric field and exhibiting a difference in the photocurrent.[27]

Some factors that might influence the detection results should be investigated, including the immunoreaction time, pH, and number of spins. The results are described in the Supporting Information (Fig. S3 and the corresponding description, ESI†). Under optimal conditions, the immunosensor showed a gradually increasing signal with the increase in the concentration of PSA, as shown in Fig. 3B. In Fig. 3C, the photocurrent showed a good liner relationship with the logarithm of PSA concentration within 0.1 ng mL^{-1}–200 ng mL^{-1} and the linear regression equation could be fitted as I (μA cm^{-2}) = −7.8994–4.6124 × lg$C$ (ng mL^{-1}) (R^2 = 0.9916, n = 8) with a detection limit (LOD) of 49.4 pg mL^{-1}. This significantly enhanced the PEC sensor performance was attributed to the introduction of ferroelectric field to induce the separation of photo-generated electron–hole pairs in the photo-active semiconductor. By comparing the results with different detection schemes for PSA (Table 1), the results showed that our PEC sensor could be comparable or even better than the previous works.

The specificity of the PEC immunoassay was validated with the interferences of common proteins or biomarkers, such as alpha-fetoprotein (AFP), carcinoembryonic antigen (CEA), bovine serum albumin (BSA) and cancer antigen 125 (CA-125). The concentrations of all interferents were set at 50 ng mL^{-1}, and the target PSA concentration of 2.0 ng mL^{-1} was used as the assay standard. As shown in Fig. 3D, the photocurrent changes induced by high-concentration non-target proteins/biomarkers were minor, while a significant photocurrent increase was achieved in the mixture including PSA, indicating the excellent interference resistance of the sensor. Such a superior signal recognition was mainly attributed to the specific recognition of the antigen and antibody. To further evaluate the accuracy and reliability of the ferroelectric BLFO-enhanced PEC sensor, we performed spiked recovery tests by doping different concentrations of PSA into clinical sample matrices that did not contain target PSA. The test results obtained from the constructed PEC sensor were compared with commercial PSA ELISA kit (Wuhan Cusabio Biotech. Inc. China, https://www.cusabio.com/). The results are shown in Table S1 (ESI†). By comparison, the average recoveries of the ferroelectric-enhanced PEC-based sensor system and the PSA ELISA kit were 94.4–104.4% and 98.2–102.9%, respectively. No significant differences were observed in the detection of real samples, indicating that the method was highly accurate and could be implemented for the clinical detection of the target PSA.

For the PEC biosensing system, which was mainly based on the photosensitive material, the output signal might be affected by various factors in the photoelectrochemical measurements. For a well-performing PEC sensor, the as-prepared photo-electrode should have good reproducibility and stability. In this case, we investigated the reproducibility and stability of the carefully prepared electrode. The results are shown in Fig. 3E and F. The photocurrent of the ferroelectric chalcogenide BLFO-modified FTO electrode was monitored during 400 s consecutive runs by regularly giving light and dark conditions, as shown in Fig. 3E. It showed that the photocurrent responses of the as-prepared electrode were very stable over 400 s and the magnitude of the photocurrent outputs were almost indistinguishable (calculated after the third light turn-on cycle). The test was repeated again for electrodes placed for long periods of time in the absence and presence of the target PSA. The results are shown in Fig. 3F. Taking 2.0 ng mL^{-1} PSA as an example, the results showed that the photocurrents could be maintained at 100.4%, 98.27%, 97.21%, and 95.90% of the initial intensity after 7, 14, 22, and 30 days, respectively (n = 3). Thus, the above results indicated that this PEC sensor had good stability and reproducibility.

Conclusions

In summary, this study describes a PEC biosensor with enhanced electron and hole separation by a ferroelectric electric field. In comparison to conventional PEC sensing platforms, the emphasis of this study is summarized as follows: (i) the introduction of the BLFO self-polarizing electric field in WO_3 nanoplates enables efficient charge separation, thereby improves the sensitivity of the PEC sensing platform; (ii) the amplification of the photocurrent is catalyzed by a split-type antigen–antibody immunoreaction to produce a sacrificial agent, thus reducing the interference in the detection system; and (iii) monolayer rGO with de-shielding effect and efficient electron conductor as a multifunctional mediating layer to build efficient PEC sensors. The strategy of effectively combining ferroelectric materials with semiconductors opens up new ways for the sensitive detection of biomarkers and disease-related biomolecules. The major objective of this study was to provide a new methodology for the enhancement of separation of photo-induced electrons and holes on PEC sensing performance. This paper revealed that the

built-in electric field of the ferroelectric perovskite effectively improved the charge separation efficiency to enhance the sensitive response of photoelectrochemical sensors, thus providing a new idea for the construction of new PEC biosensors.

Compliance with ethical standards

All the experiments were performed in accordance with the Guidelines of Fuzhou University (China), and approved by the ethics committee at Fuzhou University (China). Informed consents were obtained from human participants of this study.

Conflicts of interest

There are no conflicts to declare.

Acknowledgements

All authors acknowledge the financial support from the National Natural Science Foundation of China (21874022 & 21675029), and the Natural Science Foundation of Chongqing (cstc2020jcyj-msxmX0977).

References

1 Y. Broza, X. Zhou, M. Yuan, D. Qu, Y. Zheng, R. Vishinkin, M. Khatib, W. Wu and H. Haick, Disease detection with molecular biomarkers: From chemistry of body fluids to nature-inspired chemical sensors, *Chem. Rev.*, 2019, **119**, 11761–11817.

2 U. Zupančič, P. Jolly, P. Estrela, D. Moschou and D. E. Ingber, Graphene enabled low-noise surface chemistry for multiplexed sepsis biomarker detection in whole blood, *Adv. Funct. Mater.*, 2021, **31**, 2010638.

3 L. Zhang, Z. Luo, R. Zeng, Q. Zhou and D. Tang, All-solid-state metal-mediated Z-scheme photoelectrochemical immunoassay with enhanced photoexcited charge-separation for monitoring of prostate-specific antigen, *Biosens. Bioelectron.*, 2019, **134**, 1–7.

4 S. Lv, K. Zhang, Q. Zhou and D. Tang, Plasmonic enhanced photoelectrochemical aptasensor with D-A F8BT/g-C3N4 heterojunction and AuNPs on a 3D-printed device, *Sens. Actuators, B*, 2020, **310**, 127874.

5 M. Li, H. Wang, X. Wang, Q. Lu, H. Li, Y. Zhang and S. Yao, Ti3C2/Cu2O heterostructure based signal-off photoelectrochemical sensor for high sensitivity detection of glucose, *Biosens. Bioelectron.*, 2019, **142**, 111535.

6 J. Tan, B. Peng, L. Tang, G. Zeng, Y. Lu, J. Wang, X. Ouyang, X. Zhu, Y. Chen and H. Feng, CuS QDs/Co3O4 Polyhedra-Driven Multiple Signal Amplifications Activated h-BN Photoeletrochemical Biosensing Platform, *Anal. Chem.*, 2020, **92**, 13073–13083.

7 R. Zeng, L. Zhang, L. Su, Z. Luo, Q. Zhou and D. Tang, Photoelectrochemical bioanalysis of antibiotics on rGO-Bi2WO6-Au based on branched hybridization chain reaction, *Biosens. Bioelectron.*, 2019, **133**, 100–106.

8 C. Zhao and S. Ding, Perspective on signal amplification strategies and sensing protocols in photoelectrochemical immunoassay, *Coord. Chem. Rev.*, 2019, **391**, 1–14.

9 J. Li, P. Xiong, J. Tang, L. Liu, S. Gao, Z. Zeng, H. Xie, D. Tang and J. Zhuang, Biocatalysis-induced formation of BiOBr/Bi2S3 semiconductor heterostructures: A highly efficient strategy for establishing sensitive photoelectrochemical sensing system for organophosphorus pesticide detection, *Sens. Actuators, B*, 2021, **331**, 129451.

10 W. Zhao, J. Xu and H. Chen, Photoelectrochemical immunoassays, *Anal. Chem.*, 2018, **90**, 615–627.

11 W. Zhao, J. Xu and H. Chen, Photoelectrochemical enzymatic biosensors, *Biosens. Bioelectron.*, 2017, **92**, 294–304.

12 K. Zhang, S. Lv, Q. Zhou and D. Tang, CoOOH nanosheets-coated g-C3N4/CuInS2 nanohybrids for photoelectrochemical biosensor of carcinoembryonic antigen coupling hybridization chain reaction with etching reaction, *Sens. Actuators, B*, 2020, **307**, 127631.

13 Z. Yu, L. Huang, J. Chen, M. Li and D. Tang, Graded oxygen-doped CdS electrode for portable photoelectrochemical immunoassay of alpha-fetoprotein coupling with a digital multimeter readout, *Sens. Actuators, B*, 2021, **343**, 130136.

14 K. Zou, Y. Fu, R. Yang, X. Zhang, C. Du and J. Chen, CuO-ZnO heterojunction derived from Cu2+-doped ZIF-8: A new photoelectric material for ultrasensitive PEC immunoassay of CA125 with near-zero background noise, *Anal. Chim. Acta*, 2020, **1099**, 75–84.

15 R. Zeng, Y. Tang, L. Zhang, Z. Luo and D. Tang, Dual-readout aptasensing of antibiotic residues based on gold nanocluster-functionalized MnO2 nanosheets with target-induced etching reaction, *J. Mater. Chem. B*, 2018, **6**, 8071–8077.

16 H. Meng, P. Liu, F. Mo, M. Chen and Y. Fu, A novel ultrasensitive photoelectrochemical biosensor for detecting microRNA 21 based on cosensitization strategy and p-n heterojunction quenching mode, *Sens. Actuators, B*, 2020, **325**, 128782.

17 B. Chakraborty, R. Saha, S. Chattopadhyay, D. De, R. D. Das, M. K. Mukhopadhyay, M. Palit and C. RoyChaudhuri, Impact of surface defects in electron beam evaporated ZnO thin films on FET biosensing characteristics towards reliable PSA detection, *Appl. Surf. Sci.*, 2021, **537**, 147895.

18 K. Chuah, Y. Wu, S. Vivekchand, K. Gaus, P. Reece, A. Micolich and J. Gooding, Nanopore blockade sensors for ultrasensitive detection of proteins in complex biological samples, *Nat. Commun.*, 2019, **10**, 2109.

19 B. Li, Z. Wan, C. Wang, P. Chen, B. Huang, X. Cheng, Q. Qian, J. Li, Z. Zhang, G. Sun, B. Zhao, H. Ma, R. Wu, Z. Wei, Y. Liu, L. Liao, Y. Ye, Y. Huang, X. Xu, X. Duan, W. Ji and X. Duan, van der Waals epitaxial growth of air-stable CrSe2 nanosheets with thickness-tunable magnetic order, *Nat. Mater.*, 2021, **20**, 818–825.

20 L. M. Yu, Y. C. Zhu, Y. L. Liu, P. Qu, M. T. Xu, Q. Shen and W. W. Zhao, Ferroelectric perovskite oxide@TiO2 nanorod

heterostructures: Preparation, characterization, and application as a platform for photoelectrochemical bioanalysis, *Anal. Chem.*, 2018, **90**, 10803–10811.

21 C. Gao, H. Yu, L. Zhang, Y. Zhao, J. Xie, C. Li, K. Cui and J. Yu, Ultrasensitive Paper-Based Photoelectrochemical Sensing Platform Enabled by the Polar Charge Carriers-Created Electric Field, *Anal. Chem.*, 2020, **92**, 2902–2906.

22 A. Maity, A. K. Raychaudhuri and B. Ghosh, High sensitivity NH3 gas sensor with electrical readout made on paper with perovskite halide as sensor material, *Sci. Rep.*, 2019, **9**, 7777.

23 L. Zhu, Z. Lv, Z. Yin, M. Li and D. Tang, Digital multimeter-based point-of-care immunoassay of prostate- specific antigen coupling with a flexible photosensitive pressure sensor, *Sens. Actuators, B*, 2021, **343**, 130121.

24 L. W. Martin and A. M. Rappe, Thin-film ferroelectric materials and their applications, *Nat. Rev. Mater.*, 2016, **2**, 16087.

25 L. Qi, S. Ruan and Y. J. Zeng, Review on recent developments in 2D ferroelectrics: Theories and applications, *Adv. Mater.*, 2021, **33**, e2005098.

26 Y. Inoue, M. Okamura and K. Sato, A thin-film semiconducting titanium dioxide combined with ferroelectrics for photoassisted water decomposition, *J. Phys. Chem.*, 1985, **89**, 5184–5187.

27 X. Chen, L. German, J. Bong, Y. Yu, M. Starr, Y. Qin, Z. Ma and X. Wang, Decoupling the charge collecting and screening effects in piezotronics-regulated photoelectrochemical systems by using graphene as the charge collector, *Nano Energy*, 2018, **48**, 377–382.

28 Y. Zhang, L. Yang, Y. Zhang, Z. Ding, M. Wu, Y. Zhou, C. Diao, H. Zheng, X. Wang and Z. L. Wang, Enhanced photovoltaic performances of La-doped bismuth ferrite/zinc oxide heterojunction by coupling piezo-phototronic effect and ferroelectricity, *ACS Nano*, 2020, **14**, 10723–10732.

29 F. Li, H. Zheng, M. Zhu, X. Zhang, G. Yuan, Z. Xie, X. Li, G. Yue and W. Zhang, Photovoltaic enhancement by Au surface-plasmon effect for La doped BiFeO3 films, *J. Mater. Chem. C*, 2017, **5**, 10615–10623.

30 J. Ma, K. Mao, J. Low, Z. Wang, D. Xi, W. Zhang, H. Ju, Z. Qi, R. Long, X. Wu, L. Song and Y. Xiong, Efficient photoelectrochemical conversion of methane into ethylene glycol by WO3 nanobar arrays, *Angew. Chem., Int. Ed.*, 2021, **60**, 9357–9361.

31 V. Galstyan, N. Poli, A. D'Arco, S. Macis, S. Lupi and E. Comini, A novel approach for green synthesis of WO3 nanomaterials and their highly selective chemical sensing properties, *J. Mater. Chem. A*, 2020, **8**, 20373–20385.

32 S. Ansari, M. Ansari, S. Satsangee and R. Jain, WO3 decorated graphene nanocomposite based electrochemical sensor: A prospect for the detection of anti-anginal drug, *Anal. Chim. Acta*, 2019, **1046**, 99–109.

33 J. Sun, L. Sun, N. Han, H. Chu, S. Bai, X. Shu, R. Luo and A. Chen, rGO decorated CdS/CdO composite for detection of low concentration NO2, *Sens. Actuators, B*, 2019, **299**, 126832.

34 R. Albers, R. Bini, J. Souza, D. Machado and L. Varanda, A general one-pot synthetic strategy to reduced graphene oxide (rGO) and rGO-nanoparticle hybrid materials, *Carbon*, 2019, **143**, 73–84.

35 G. Luo, L. Shen, J. Zheng and C. Xu, A europium ion doped WO3 film with the bi-functionality of enhanced electrochromic switching and tunable red emission, *J. Mater. Chem. C*, 2017, **5**, 3488–3494.

36 J. Shah, H. Ye, Y. Liu, A. Idris, A. Malik, Y. Zhang, H. Han and C. Li, Exploration of the intrinsic factors limiting the photocurrent density in ferroelectric BiFeO3 thin film, *J. Mater. Chem. A*, 2020, **8**, 6863–6873.

37 Y. Lin, Q. Wang, S. Gao, H. Yang and L. Wang, Constructing flower-like porous Bi0.9La0.1FeO3 microspheres for excellent electromagnetic wave absorption performances, *J. Alloys Compd.*, 2018, **745**, 761–772.

38 R. Gao, C. Fu, W. Cai, G. Chen, X. Deng and X. Cao, Switchable photovoltaic effect in Au/Bi0.9La0.1FeO3/La0.7Sr0.3MnO3 heterostructures, *Mater. Chem. Phys.*, 2016, **181**, 277–283.

39 D. Liang, J. Luo, Y. Huang, X. Liang, X. Qiu, J. Wang and M. Yang, A porous carbon nitride modified with cobalt phosphide as an efficient visible-light harvesting nanocomposite for photoelectrochemical enzymatic sensing of glucose, *Microchim. Acta*, 2019, **186**, 856.

40 B. Zhao, P. Miao, Z. Hu, X. Zhang, X. Geng, Y. Chen and L. Feng, Signal-on electrochemical aptasensors with different target-induced conformations for prostate specific antigen detection, *Anal. Chim. Acta*, 2021, **1152**, 338282.

41 S. Hu, H. Xu, B. Zhou, S. Xu, B. Shen, B. Dong, Z. Yin, S. Xu, L. Sun, J. Lv, J. Wang, W. Xu, X. Bai, L. Xu, S. Mintova and H. Song, Double stopband bilayer photonic crystal based upconversion fluorescence PSA sensor, *Sens. Actuators, B*, 2021, **326**, 128816.

42 J. Chen, F. Xue, Z. Yu, L. Huang and D. Tang, A polypyrrole-polydimethylsiloxane sponge-based compressible capacitance sensor with molecular recognition for point-of-care immunoassay, *Analyst*, 2020, **145**, 7186–7190.

43 E. Wajs, G. Rughoobur, K. Burling, A. George, A. Flewitt and V. Gnanapragasam, A novel split mode TFBAR device for quantitative measurements of prostate specific antigen in a small sample of whole blood, *Nanoscale*, 2020, **12**, 9647–9652.

44 A. Ouhibi, A. Raouafi, N. Lorrain, M. Guendouz, N. Raouafi and A. Moadhen, Functionalized SERS substrate based on silicon nanowires for rapid detection of prostate specific antigen, *Sens. Actuators, B*, 2021, **330**, 129352.

45 G. Cai, Z. Yu, R. Ren and D. Tang, Exciton–plasmon interaction between AuNPs/graphene nanohybrids and CdS quantum dots/TiO2 for photoelectrochemical aptasensing of prostate-specific antigen, *ACS Sens.*, 2018, **3**, 632–639.

46 K. Zhang, S. Lv, M. Lu and D. Tang, Photoelectrochemical biosensing of disease marker on p-type Cu-doped Zn0.3Cd0.7S based on RCA and exonuclease III amplification, *Biosens. Bioelectron.*, 2018, **117**, 590–596.

